

On Shear Locking in MLPG Solid-Shell Approach

T. Jarak¹ and J. Sorić¹

Abstract: A solid-shell MLPG approach for the numerical analysis of plates and shells is presented. A special attention is devoted to the transversal shear locking effect that appears in the structure thin limit. The theoretical origins of shear locking in the purely displacement-based approach are analyzed by means of the consistency paradigm. It is shown that the spurious constraints appear in the constrained strain field, which lead to the appearance of shear locking and sub-optimal convergence rates. The behaviour of the mixed MLPG approach in the thin limit is also considered. It is determined that in the mixed paradigm the Kirchhoff-Love conditions have to be satisfied only at the nodes to avoid the shear locking effects. The validity of the theoretical predictions is supported by the presented numerical examples, where good convergence and accuracy are obtained even if the low-order meshless approximations are used.

Keywords: MLPG method, solid-shell, thin plate and shells, shear locking.

1 Introduction

Meshless methods have attracted considerable attention in the academic community dealing with the numerical modeling of plate and shell structures due to the ability of meshless approximation schemes to produce the interpolation field of a high continuity order in a simple and straightforward manner. This convenience has often been used for Kirchhoff plates and shells [Krysl and Belytschko (1996); Sladek, Sladek and Mang (2002); Liu, Liu and Tan (2002); Rabczuk, Areias and Belytschko (2007)].

In meshless methods, the Reissner-Mindlin kinematic assumptions, which take into account the transversal shear deformations, are employed most often to describe the shell kinematics [Donning and Liu (1998); Garcia, Fancello, de Barcellos and Duarte (2000); Noguchi, Kawashima and Miyamura (2000); Kim, Choi, Chen and Botkin (2002); Chen and Wang: (2006); Sladek, Sladek, Zhang, Krivacek and Wen (2006)]. Such algorithms are capable of achieving excellent results, but they

¹ Faculty of Mechanical Engineering and Naval Architecture, University of Zagreb, Croatia

possess the rotational degrees of freedom (DOFs) and involve a reduction of a material law. This may lead to certain complications when describing the boundary conditions (BCs), or when connecting such models to 3-D solid algorithms. To resolve these problems, the solid-shell concept, well known from the Finite Element Method (FEM) [Sze (2002); Tan and Vu-Quoc (2005); Klinkel, Grutmann, Wagner (2006)], has been applied in the frame of the MLPG method [Jarak, Sorić and Hoster (2007)]. Therein, only the nodal translational DOFs are used, and the meshless approximations are applied only in the in-plane tangential directions. This is computationally more efficient than using meshless 3-D approximations, which are necessary in the meshless formulations based on a direct 3-D solid approach, such as [Li, Hao and Liu (2000)].

The appearance of locking phenomena poses a serious obstacle in the meshless formulations for shell-like structures. Unfortunately, the methods for their elimination developed in the frame of the FEM technology, such as various assumed strain or reduced integration methods [Hughes (1987); Zienkiewicz, Taylor and Zhu (2005)], are not directly applicable to the meshless methods, mainly due to the non-polynomial character of meshless approximation functions. Therefore, alternative procedures for the alleviation of the locking effects have been proposed for the meshless methods. In the purely displacement-based (primal) formulations, the raising of the p -basis order in meshless interpolations is often employed. Krysl and Belytschko used this technique with the Moving Least Squares (MLS) approximation scheme in order to alleviate membrane locking in their EFG formulation for Kirchhoff shells [Krysl and Belytschko (1996)]. Similar approach has been applied as a remedy against shear locking when employing the functions with the p -capability, such as the hp -clouds method [Garcia, Fancello, de Barcellos and Duarte (2000)], the MLS method [Noguchi, Kawashima and Miyamura (2000)], or the Point Interpolation Method (PIM) [Liu, Chua and Ghista (2007)]. Such p -refinement can be done straightforwardly without increasing the total number of global DOFs, but it only alleviates locking and produces significant computational costs needed for the computation of meshless functions of a higher order.

The use of the consistency approach to circumvent the shear locking effects has also been proposed, wherein the rotation field shape functions are constructed by differentiating the displacements shape functions [Donning and Liu (1998); Kanok-Nukulchai, Barry, Saran-Yasootorn and Bouillard (2001)]. However, it has been proved in [Tiago and Leitão (2007)] that such an approach may yield a rank deficient global system of equations within the Galerkin method, because the approximation functions for the rotation field are linearly dependent.

The classical mixed approaches were first employed in meshless formulations for the elimination of volumetric locking. This is usually accomplished by approximati-

ing the pressure and displacement fields separately, as in [Dolbow and Belytschko (1999), De and Bathe (2001)], and the references therein. However, because in classical mixed approaches Lagrangian multipliers are involved in the underlying multi-field variational principles, the complicated inf-sup condition [Bathe (2001)] must be satisfied, which ensures the stability of solutions. Due to the complicated nature of meshless approximations, in general it is not possible to prove analytically whether a model passes this condition. Therefore, [BaniHani and De (2009)] performed the numerical inf-sup test for a shear-deformable plate formulation based on the Method of Finite Spheres (MFS) [De and Bathe (2000)]. Similarly to mixed FE formulations, it has been shown that the passing of the inf-sup test disqualifies an arbitrary choice of the approximation functions used for independent fields, and that only the models that pass the inf-sup tests are locking-free and exhibit near-optimal convergence. Alternative “assumed strain” meshless techniques suitable for eliminating shear locking include a change of independent field variables [Cho and Atluri (2001); Li, Sorić, Jarak and Atluri (2005)], and the Stabilized Nodal Conforming Integration (SNCI) method [Wang and Chen (2004); Chen and Wang (2006)]. The switch of independent variables does not increase the total number of DOFs, but it raises the order of the derivatives of meshless functions under integrals. The SNCI method utilizes the curvature smoothing to eliminate shear locking. It avoids the Gaussian integration of global weak forms due to the nodal integration and passes the linear patch test exactly, but the problems with spurious modes may appear [Puso, Chen, Zywicz and Elmer (2007)]. Furthermore, the SNCI method usually requires the Voronoi tessellation of a global domain for defining the congruent integration cells, which is a procedure similar to creating a global mesh of triangular elements. Therefore, this is not a truly meshless concept. In order to avoid such complications, Atluri and coworkers proposed a mixed Meshless Local Petrov-Galerkin (MLPG) paradigm [Atluri, Han and Rajendran (2004)]. The MLPG method, originally proposed in [Atluri and Zhu (1998)], is a truly meshless method, because theoretically, both the approximation of variables and the numerical integration of governing equations may be performed without using the global meshes of adjacent background cells. Due to the underlying weighted local Petrov-Galerkin principle, the MLPG method is a very general platform that may be used for deriving other truly meshless methods [Atluri (2004)], including the MFS method. In the mixed MLPG approach, other field variables may be approximated separately besides the displacement field. The local weak forms (LWF) of governing equations are written in terms of these additional variables only, and their nodal values are then eliminated from the equations by enforcing their compatibility with the approximated displacements at the nodes. In this way, the use of the Lagrangian multipliers and the problems associated with the inf-sup conditions are

avoided. Consequently, all unknown field variables may be approximated by the same meshless functions. The mixed paradigm is computationally superior to the comparable primal meshless approaches because it avoids the differentiation of the shape functions at each integration point, and decreases the continuity requirements for the trial functions. This approach has since then shown great potential in efficiently solving various engineering problems, including high-speed impact, contact and penetration problems [Han, Rajendran and Atluri (2005)], the analysis of thin beams, plates and shells [Jarak and Sorić (2008), Sorić and Jarak (2010); Moosavi, Delfanian, and Khelil (2011)], the topology-optimization of 2-D structures [Li and Atluri (2008)], or elastodynamic problems [Moosavi and Khelil (2009)].

The aim of this contribution is to reveal the behaviour of the primal and mixed MLPG solid-shell approaches, originally developed in [Jarak, Sorić and Hoster (2007); Sorić and Jarak (2010)], in the thin structure limit. For that purpose, some concepts from the consistency paradigm [Prathap (1993)] are borrowed. All algorithms are based on the 3-D solid-shell concept, which allows the implementation of complete 3-D constitutive models. Discretization is carried out by the couples of nodes located on the upper and lower structure surfaces, and the governing equations are derived from the LWF of the 3-D equilibrium equations, defined around the node couples. All independent field variables are approximated by using the same MLS approximation functions in the tangential in-plane directions. In the mixed formulation, strain components are approximated separately from displacements, and their nodal values are eliminated from the global system of equations by enforcing the compatibility conditions between the strains and displacements at the nodes. In the primal approach, Poisson's thickness locking is overcome by adopting the hierarchical quadratic interpolation for the transversal displacement component [Hauptmann and Schweizerhof (1998)], as in [Jarak, Sorić and Hoster (2007)], while a change of variables is employed in the mixed approach [Sorić and Jarak (2010)].

The paper is organized as follows: Section 2 briefly describes some relevant details of the MLS approximation scheme. The derivation of the governing equations is presented in Section 3, together with some information concerning the numerical implementation and the elimination of the thickness locking effect. Section 4 deals with the theoretical considerations about transversal shear locking in both the primal and mixed solid-shell approach. The validity of the presented theoretical predictions, as well as the efficiency of the mixed strategy in the thin structure limit, is demonstrated by numerical examples in Section 5. Concluding remarks are given in Section 6.

2 MLS approximation

One of the most popular approximation tools in meshless methods is the Moving Least Squares (MLS) scheme [Lancaster and Salkauskas (1986)]. The MLS approximant $f^{(h)}(\mathbf{X})$, which approximates the function $f(\mathbf{X})$ in the domain Ω for a set of randomly scattered points $\mathbf{X}_J = 1, 2, \dots, N$, may be written as

$$f^{(h)}(\mathbf{X}) = \mathbf{p}^T(\mathbf{X}) \mathbf{a}(\mathbf{X}), \quad (1)$$

where $\mathbf{p}(\mathbf{X})$ is a vector of basis functions. A complete monomial p-basis is usually used in order to ensure the consistency of the approximations. For a 2-D space, the complete linear monomial basis is defined as

$$\mathbf{p}^T(\mathbf{X}) = [1 \quad X^1 \quad X^2], \quad (2)$$

while the quadratic basis reads as

$$\mathbf{p}^T(\mathbf{X}) = [1 \quad X^1 \quad X^2 \quad (X^1)^2 \quad X^1 X^2 \quad (X^2)^2]. \quad (3)$$

The vector $\mathbf{a}(\mathbf{X})$ contains the unknown coefficients which are the functions of \mathbf{X} . After calculating $\mathbf{a}(\mathbf{X})$, which is determined by minimizing certain discrete weighted L_2 norm, as described in detail in [Atluri (2004)], the MLS approximation may be written in the form similar to that usually used in FEM as

$$f^{(h)}(\mathbf{X}) = \sum_{J=1}^n \phi_J(\mathbf{X}) \hat{f}_J, \quad (4)$$

where $\phi_J(\mathbf{X})$ is the shape function associated with the node \mathbf{X}_J ,

$$\phi_J(\mathbf{X}) = \sum_{i=1}^m p_i(\mathbf{X}) [\mathbf{A}^{-1}(\mathbf{X}) \mathbf{B}(\mathbf{X})]_{iJ}. \quad (5)$$

$p_i(\mathbf{X})$ stands for the terms of the monomial p-base, and matrices \mathbf{A} and \mathbf{B} are defined as

$$\begin{aligned} \mathbf{A} &= \sum_{J=1}^n W_J(\mathbf{X}) \mathbf{p}(\mathbf{X}_J) \mathbf{p}^T(\mathbf{X}_J), \\ \mathbf{B} &= [W_1(\mathbf{X}) \mathbf{p}(\mathbf{X}_1) \quad W_2(\mathbf{X}) \mathbf{p}(\mathbf{X}_2) \quad \cdots \quad W_J(\mathbf{X}) \mathbf{p}(\mathbf{X}_J) \quad \cdots \quad W_n(\mathbf{X}) \mathbf{p}(\mathbf{X}_n)]. \end{aligned} \quad (6)$$

Herein, $W_J(\mathbf{X}); J = 1, 2, \dots, n$ denotes the weight functions associated with the nodes whose weight functions do not vanish at \mathbf{X} , i.e., $W_J(\mathbf{X}) \neq 0$, and n is the

total number of such nodes for \mathbf{X} . The choice of the weight functions is important because some important properties of the MLS approximants are inherent to the properties of its weight function, e.g., the support domain of $\phi_J(\mathbf{X})$ coincides with the support domain of $W_J(\mathbf{X})$, and the order of the continuity of $f^{(h)}(\mathbf{X})$ is usually equal to that of the applied weight functions.

In this work, the fourth-order spline-type weight function, described in detail in [Atluri(2004)], is used in the primal MLPG formulation. In that case, the MLS approximants do not interpolate the given values at the nodes, $f^{(h)}(\mathbf{X}_J) \neq \hat{f}_J$. Therefore, the modified collocation procedure [Zhu and Atluri (1998)] is used here to satisfy the essential BCs when employing the spline-type weight functions. In order to avoid such complications, the regularized weight functions have been proposed, whose application leads to the MLS shape functions which satisfy the Kronecker delta property at the nodes with high accuracy, i.e., $\phi_J(\mathbf{X}_I) \approx \delta_{JI}$ [Most and Bucher (2005); Most (2007)]. In this contribution, the regularized weight function presented in [Sorić and Jarak (2010)] is applied in the mixed MLPG algorithms. It enables the direct imposition of the essential BCs, like in FEM. In addition, it has been noticed that such MLS functions are less dependant on the size of the support domain of $W_J(\mathbf{X})$ than the MLS approximations employing the spline-type weight functions.

3 MLPG solid-shell concept

3.1 Geometry, kinematics and constitutive relations

In the solid-shell concept, the kinematics of shell structures are described by the displacements associated with the couples of material points. The points of the same couple are positioned on the upper and bottom structure surface and lie on the same material fibre that is initially normal to the structure middle surface. During a deformation process, the fibre remains straight, but not necessarily normal to the middle surface. Such model retains the Mindlin-Reissner kinematic assumptions, while at the same time allows the change of the structure thickness. A 3-D shell geometry is described by

$$\mathbf{X}(\theta^j) = X^i(\theta^j) \mathbf{e}_i = \psi^1(\theta^3) \mathbf{X}_{(u)}(\theta^\alpha) + \psi^2(\theta^3) \mathbf{X}_{(l)}(\theta^\alpha) \tag{7}$$

with the functions ψ^1 and ψ^2 defined as

$$\psi^1(\theta^3) = \frac{1}{2} + \frac{\theta^3}{h}, \quad \psi^2(\theta^3) = \frac{1}{2} - \frac{\theta^3}{h}. \tag{8}$$

Herein \mathbf{e}_i denotes the unit vectors in the global Cartesian coordinate system, while $\mathbf{X}_{(u)}$ and $\mathbf{X}_{(l)}$ are the position vectors associated with the upper and lower structure surface, respectively, see Fig. 1.

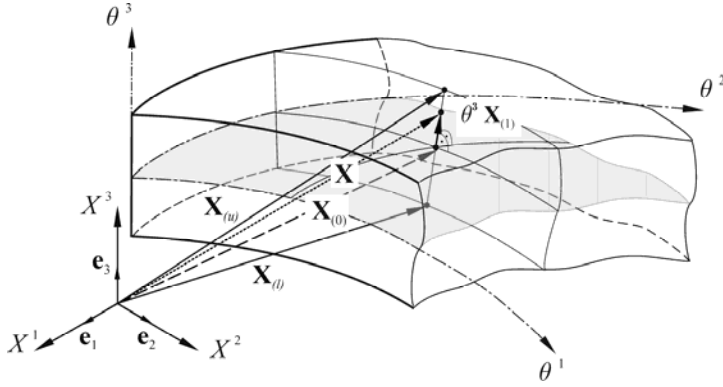


Figure 1: Geometry description of shell continuum

The shell is parameterized by the curvilinear coordinates θ^j , with θ^α as the middle surface coordinates, and $\theta^3 \in [-h/2, h/2]$ as the local coordinate in the thickness direction, i.e., in the direction normal to the middle surface. h stands for the shell thickness. The Greek indices take the values 1 or 2, and the Latin indices represent the numbers 1, 2 or 3, unless not specified otherwise.

Similarly to [Parisch (1995); Kim, Liu and Han (2005)], relation (7) may be rewritten in the form used in the degenerated shell concept as

$$\mathbf{X}(\theta^j) = \mathbf{X}_{(0)}(\theta^\alpha) + \theta^3 \mathbf{X}_{(1)}(\theta^\alpha) \quad (9)$$

with $\mathbf{X}_{(0)} = (\mathbf{X}_{(u)} + \mathbf{X}_{(l)})/2$ as the middle surface position vector and $\mathbf{X}_{(1)} = (\mathbf{X}_{(u)} - \mathbf{X}_{(l)})/h$ as the unit shell director.

Analogously to the position vector \mathbf{X} , the linear distribution over the thickness is assumed for all displacement components,

$$\mathbf{u}(\theta^j) = u^i(\theta^j) \mathbf{e}_i = \psi^1(\theta^3) \mathbf{u}_{(u)}(\theta^\alpha) + \psi^2(\theta^3) \mathbf{u}_{(l)}(\theta^\alpha), \quad (10)$$

where $\mathbf{u}_{(u)}$ and $\mathbf{u}_{(l)}$ are the displacement vectors associated with the points on the upper and lower surfaces, respectively. The vector \mathbf{u} may be written in terms of the variables associated with the middle surface as

$$\mathbf{u}(\theta^j) = \mathbf{u}_{(0)}(\theta^\alpha) + \theta^3 \mathbf{u}_{(1)}(\theta^\alpha). \quad (11)$$

Herein, $\mathbf{u}_{(0)} = (\mathbf{u}_{(u)} + \mathbf{u}_{(l)})/2$ stands for the middle surface displacement vector, while $\mathbf{u}_{(1)} = (\mathbf{u}_{(u)} - \mathbf{u}_{(l)})/h$ describes the total rotations.

The strain tensor is calculated from the displacements by the relation

$$\boldsymbol{\varepsilon} = \varepsilon_{ij} \mathbf{G}^i \otimes \mathbf{G}^j = \frac{1}{2} (\mathbf{G}_i \cdot \mathbf{u}_{,\theta^j} + \mathbf{G}_j \cdot \mathbf{u}_{,\theta^i}) \mathbf{G}^i \otimes \mathbf{G}^j, \tag{12}$$

and the complete stress tensor $\boldsymbol{\sigma}$ may be obtained by employing the Hooke's law for linear elastic isotropic homogeneous materials. It is important to stress that no reduction of the 3-D material law is present in the solid-shell approach. The stress vector \mathbf{t} acting over a boundary surface $\partial\Omega$ is computed by

$$\mathbf{t} = \mathbf{n} \boldsymbol{\sigma}, \tag{13}$$

with \mathbf{n} as the outward unit normal vector to $\partial\Omega$.

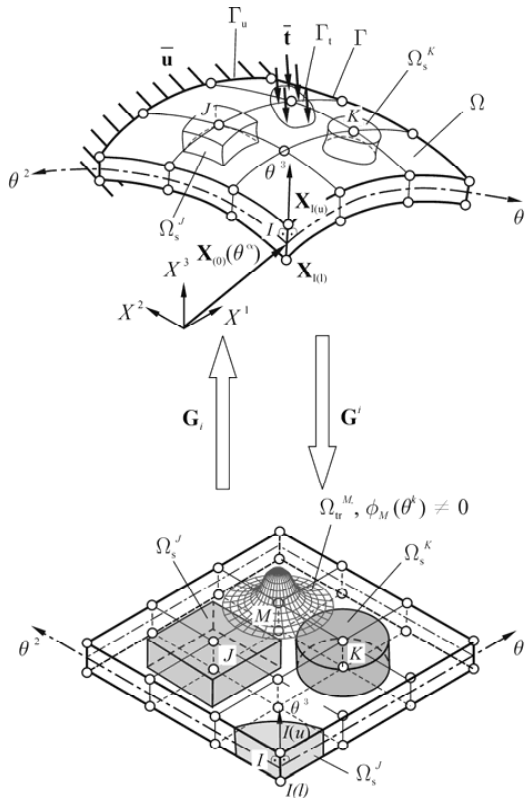


Figure 2: Parameterization and discretization of numerical model

3.2 Governing equations

The stationary state of a linear elastic shell is examined, considered here as a 3-D solid continuum represented by a global domain Ω , as illustrated in Fig. 2. The 3-D equilibrium equations, written in the global Cartesian coordinate system,

$$\sigma_{,X^j}^{ij} + b^i = 0, \text{ in } \Omega, \quad (14)$$

represent the strong form of governing equations. In the above equation, b^j are the components of the body force vector $\mathbf{b} = b^j \mathbf{e}_j$, and σ^{ij} denotes the components of the stress tensor in the global Cartesian coordinate system, $\boldsymbol{\sigma} = \sigma^{ij} \mathbf{e}_i \otimes \mathbf{e}_j$.

The global domain Ω is bounded by the global boundary Γ , $\Gamma = \Gamma_u \cup \Gamma_t$, on which the following boundary conditions (BCs) are prescribed

$$u^i = \bar{u}^i, \text{ on } \Gamma_u, \quad (15)$$

$$t^i = \sigma^{ij} n_j = \bar{t}^i, \text{ on } \Gamma_t. \quad (16)$$

Herein Γ_u and Γ_t are the parts of Γ with the prescribed displacements \bar{u}^i and surface tractions \bar{t}^i , respectively, while n_j denotes the direction cosines of the unit outward normal vector to Γ , $\mathbf{n} = n_j \mathbf{e}^j$. The shell middle surface is parameterized by using curvilinear coordinates θ^α . Thus, the shell continuum is mapped into the parametric space $(\theta^1, \theta^2, \theta^3)$ and discretized by a set of node couples $I = 1, 2, \dots, N$, with N as the total number of the node couples used for discretization. The nodes $I(u)$ and $I(l)$ forming a node couple I are positioned on the upper and lower shell surface, respectively, as shown in Fig. 2, and their respective position vectors in the global Cartesian system are $\mathbf{X}_{I(u)}$ and $\mathbf{X}_{I(l)}$. According to the local Petrov-Galerkin approach, around each node couple a small region called a local sub-domain is defined, with the couple positioned at its centre. The local sub-domains are represented by their volumes Ω_s^I , and are bounded by the local boundaries $\partial\Omega_s^I$. Theoretically, Ω_s^I may be of arbitrary size and shape, and are allowed to overlap each other under the condition that their union covers the entire computational region. For simplicity, in this work Ω_s^I are the parallelepipeds in the parametric space, and their vertical axes are parallel to the θ^3 -direction, as in Fig. 2.

In general, the local boundary $\partial\Omega_s^I$ can be split into three parts,

$$\partial\Omega_s^I = L_s^I \cup \Gamma_{st}^I \cup \Gamma_{su}^I, \quad \Gamma_{st}^I = \Gamma_t \cap \partial\Omega_s^I, \quad \Gamma_{su}^I = \Gamma_u \cap \partial\Omega_s^I, \quad (17)$$

where L_s^I is the part of $\partial\Omega_s^I$ which is entirely inside Ω , and Γ_{st}^I and Γ_{su}^I are the parts of $\partial\Omega_s^I$ which coincide with Γ_t and Γ_u , respectively.

The equilibrium equations (15) may be written in the local weak form (LWF) over each local sub-domain as

$$\int_{\Omega_s^I} v_{ki} \left(\sigma_{,X^j}^{ij} + b^i \right) d\Omega = 0, \quad I = 1, 2, \dots, N. \tag{18}$$

Herein $v_{ki}; k = 1, 2, 3$, describes three linearly independent sets of kinematically admissible test functions. These sets have to result in a sufficient number of meaningful equations, as explained in detail in [Atluri and Zhu (2000)]. For simplicity, they can be formed as

$$v_{ki} = \delta_{ki} v \left(\theta^j \right), \tag{19}$$

where δ_{ki} is the Kronecker delta symbol and v denotes an arbitrary admissible test function. In the solid-shell approach, six displacement variables, $u_{(u)}^i$ and $u_{(l)}^i$, are needed to describe the linear displacement distribution over the thickness. Therefore, six independent equations per each local sub-domain are required, one for each unknown displacement field variable. Here they are obtained by assuming the test functions that are linear over the thickness,

$$v \left(\theta^k \right) = \begin{cases} c_1 + c_2 \theta^3, & \theta^k \in \Omega_s^I \cup \partial\Omega_s^I \\ 0, & \theta^k \notin \Omega_s^I \cup \partial\Omega_s^I \end{cases} \tag{20}$$

with c_1 and c_2 as arbitrarily chosen non-zero real constants, $c_1, c_2 \in \mathbb{R}$.

By employing the divergence theorem, taking (13) on $\partial\Omega_s^I$ into account, employing the decomposition of $\partial\Omega_s^I$ according to (17), and enforcing the natural BC (16) on Γ_{st} , the LWF (18) may be transformed to the following form

$$\begin{aligned} - \int_{L_s^I} n_j \sigma^{kj} d\Gamma - \int_{\Gamma_{su}^I} n_j \sigma^{kj} d\Gamma &= \int_{\Omega_s^I} b^k d\Omega + \int_{\Gamma_{st}^I} \bar{t}^k d\Gamma, \\ \int_{\Omega_s^I} \theta_{,X^j}^3 \sigma^{kj} d\Omega - \int_{L_s^I} \theta^3 n_j \sigma^{kj} d\Gamma - \int_{\Gamma_{su}^I} \theta^3 n_j \sigma^{kj} d\Gamma &= \int_{\Omega_s^I} \theta^3 b^k d\Omega + \int_{\Gamma_{st}^I} \theta^3 \bar{t}^k d\Gamma. \end{aligned} \tag{21}$$

For a more detailed information on the derivation of expression (21), the reader is referred to [Sorić and Jarak (2010)]. The first and the second expressions in (21) are associated with the constant and linear term of the test function (20), respectively. Relations (21) serve as the starting point in developing various primal and mixed MLPG solid-shell formulations.

3.2.1 Primal solid-shell approach

In the primal numerical formulations, the displacement field appears as the only unknown independent field. By means of the kinematic relations (12), the stress tensor $\boldsymbol{\sigma} = \sigma^{ij} \mathbf{G}_i \otimes \mathbf{G}_j$ can be computed as

$$\sigma^{ij} = C^{ijkl} \frac{1}{2} \left(\mathbf{G}_i \cdot \mathbf{u}_{,\theta^j}^{(h)} + \mathbf{G}_j \cdot \mathbf{u}_{,\theta^i}^{(h)} \right), \quad (22)$$

where C^{ijkl} refers to the components of the material tensor $\mathbf{C} = C^{ijkl} \mathbf{G}_i \otimes \mathbf{G}_j \otimes \mathbf{G}_k \otimes \mathbf{G}_l$, and $\mathbf{u}^{(h)}$ denotes the approximated displacement field. After transforming the stress tensor into the global Cartesian coordinate system, and by inserting it into (21), the LWF for each local sub-domain may be obtained. In the above expressions, the derivatives of the displacements appear, which is computationally expensive due to the high costs associated with the calculation and numerical integration of the derivatives of MLS functions. More details on the primal MLPG formulation can be found in [Jarak, Sorić and Hoster (2007)].

3.2.2 Mixed solid-shell approach

In contrast to the primal MLPG formulations, in the mixed MLPG strategy some additional field variables, such as strain or stress components, are approximated separately from displacements. For clearness, we follow the approach presented in [Jarak and Sorić (2008)], where all displacement and strain components are distributed linearly across the thickness as

$$\begin{aligned} u^{i(h)}(\theta^k) &= \psi^1(\theta^3) u_{i(u)}^{i(h)}(\theta^\alpha) + \psi^2(\theta^3) u_{i(l)}^{i(h)}(\theta^\alpha), \\ \varepsilon_{ij}^{(h)}(\theta^k) &= \psi^1(\theta^3) \varepsilon_{ij(u)}^{(h)}(\theta^\alpha) + \psi^2(\theta^3) \varepsilon_{ij(l)}^{(h)}(\theta^\alpha). \end{aligned} \quad (23)$$

Herein $\varepsilon_{ij(u)}^{(h)}$, $\varepsilon_{ij(l)}^{(h)}$ and $u_{i(u)}^{(h)}$, $u_{i(l)}^{(h)}$ denote the approximants of the strains and displacements on the upper and lower plate surface, respectively. The stress tensor $\boldsymbol{\sigma} = \sigma^{ij} \mathbf{G}_i \otimes \mathbf{G}_j$ is computed directly from the approximated strains by the constitutive relation

$$\sigma^{ij} = C^{ijkl} \varepsilon_{kl}^{(h)}. \quad (24)$$

LWF is obtained by transforming the stress tensor (24) into the global Cartesian coordinate system, and by inserting it into (21). To derive a closed system of equations at a structural level, the 3-D kinematic relations (12) are imposed only at the

nodes,

$$\begin{aligned}\varepsilon_{ij}^{(h)}(\mathbf{X}_{(u)}^I) &\approx \hat{\varepsilon}_{ij(u)}^I = \frac{1}{2} \left(\mathbf{G}_i \cdot \mathbf{u}_{,\theta^j}^{(h)} + \mathbf{G}_j \cdot \mathbf{u}_{,\theta^i}^{(h)} \right) \Big|_{\mathbf{X}_{(u)}}, \\ \varepsilon_{ij}^{(h)}(\mathbf{X}_{(l)}^I) &\approx \hat{\varepsilon}_{ij(l)}^I = \frac{1}{2} \left(\mathbf{G}_i \cdot \mathbf{u}_{,\theta^j}^{(h)} + \mathbf{G}_j \cdot \mathbf{u}_{,\theta^i}^{(h)} \right) \Big|_{\mathbf{X}_{(l)}}.\end{aligned}\quad (25)$$

Note that the assumptions about the interpolation of the nodal strain values will be satisfied with high accuracy if the interpolating MLS (IMLS) functions from [Sorić and Jarak (2010)] are used. By inserting the discretized form of relations (25) into the discretized LWF, a system of discretized linear equations may be obtained, where only the nodal displacements appear as unknown variables, as explained in detail in [Jarak and Sorić (2008); Sorić and Jarak (2010)].

3.3 Poisson's thickness locking

It is well known from the FE literature that the classical displacement-based numerical shell models based on the 3-D continuum kinematics are plagued by the Poisson's thickness locking effect if the linear distribution of the transversal displacement component over the thickness is assumed. In such cases, the normal transversal strain component does not vary through the thickness, and locking arises if the Poisson's coefficient is different from zero. In the meshless methods, this locking effect may be avoided by utilizing higher-order shell theories, as in [Qian, Batra, and Chen (2003)], or a direct 3-D continuum approach [Li, Hao and Liu (2000)], but such formulations are computationally costly and time-consuming due to the large number of DOFs over the thickness.

In the primal approach presented in this work, the hierarchical quadratic interpolation for the transversal displacement component, proposed in [Hauptmann and Schweizerhof (1998)], is applied to eliminate the thickness locking effect. This strategy increases the number of unknowns at the global level, because it involves the additional unknown displacement parameters associated with the quadratic term. A closed system of equations is obtained by employing the test functions that are quadratic in the thickness direction [Jarak, Sorić and Hoster (2007)].

In the mixed approach, the change of variables is employed, whereby the transversal normal strain component is replaced by the transversal normal stress component as the independent variable, as presented in detail in [Sorić, Jarak (2010)]. It should be stressed that this procedure does not affect the behavior of the mixed formulation in the thin structure limit with respect to shear locking.

4 Transversal shear locking in the MLPG solid-shell concept

In [Li, Sorić, Jarak and Atluri. (2005)], the origin of the shear locking effect was analyzed in a primal plate MLPG formulation based on the solid-shell concept. By inspecting the expressions of the LWF associated with the sub-domains Ω_s^I that do not intersect the plate boundary edges, it was showed that the inconsistent constraints for rotations might appear in the thin plate limit. Thereby, the assumption about the MLS functions being approximately polynomials over Ω_s^I was introduced, which holds only if Ω_s^I is sufficiently small. Furthermore, no detailed analysis was made to clarify how the raising of the MLS p-basis order affects shear locking.

In this contribution, a more systematic analysis is performed by borrowing some concepts from the consistency paradigm [Prathap (1993)], used in FEM to develop field-consistent elements free of locking effects. In the consistency paradigm, it is required that the approximation functions used for generalized displacement variables do not cause any spurious constraints in the penalty-linked strain fields. Otherwise, a formulation locks to the erroneous results, or produces sub-optimal convergence rates.

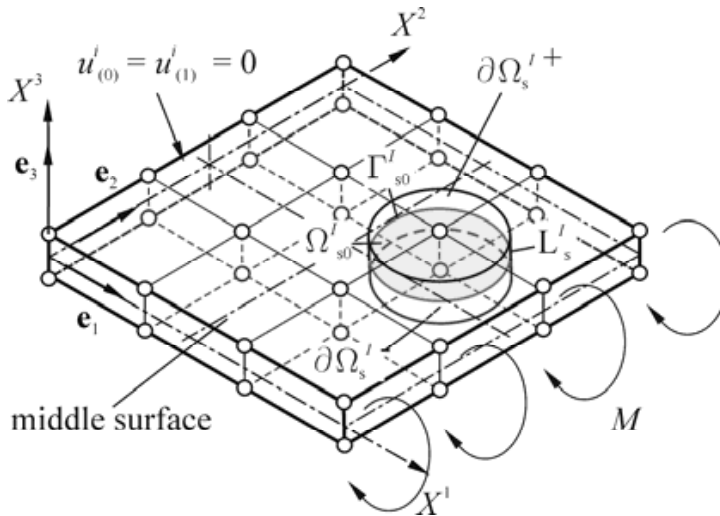


Figure 3: Rectangular thin plate subjected to pure bending with Ω_s^I for an internal node couple I

For clarity of the subsequent discussion, a rectangular thin plate with $\theta^k = X^k$ is considered. The plate is clamped along the edge $X^1 = 0$, and is subjected to the constant moment load at the opposite boundary edge, as shown in Fig. 3. The

global Cartesian coordinate system with the unit vectors \mathbf{e}_i is attached to the plate. The following assumptions are introduced:

1. Body forces are neglected, $b^i = 0$.
2. The Poisson's thickness locking effect is not considered here, and therefore, the value of the Poisson's coefficient is set to zero, i.e., $\nu = 0$.
3. All generalized displacement variables are approximated by the same MLS functions.
4. In order to avoid the influence of the BCs, the LWF for an internal local sub-domain Ω_s^I that does not intersect the plate boundary edges is analyzed. Then, $\Gamma_{su}^I = \partial\Omega_s^I \cap \Gamma_u \in \emptyset$, and $\bar{t}_i = 0$ on $\Gamma_{st}^I = \partial\Omega_s^{I+} \cup \partial\Omega_s^{I-}$, where $\partial\Omega_s^{I+}$ and $\partial\Omega_s^{I-}$ are the parts of $\partial\Omega_s^I$ that coincide with the upper and lower plate surface, respectively, according to Fig. 3.
5. The side surfaces of Ω_s^I , denoted as L_s^I , are perpendicular to the X^1, X^2 -plane, and therefore, $n_3 = 0$ for the outward unit normal vector on L_s^I .

It is to note that the assumptions 1 and 2 lead to the pure bending state. According to [Timoshenko and Goodier (1970)], the exact solutions for the generalized displacements may be written as

$$u_{(0)}^{3(e)} = -k_1 (X^1)^2, \quad u_{(1)}^{1(e)} = -u_{(0),X^3}^{3(e)} = k_2 X^1, \quad u_{(0)}^{1(e)} = u_{(0)}^{2(e)} = u_{(1)}^{2(e)} = u_{(1)}^{3(e)} = 0. \quad (26)$$

According to (11), $u_{(0)}^i$ are the Cartesian global components of the middle surface displacement vector, while $u_{(1)}^i$ describe rotations. Furthermore, the strain and stress components may be expressed as $\epsilon_{11}^{(e)} = u_{(1)}^{1(e)} = k_2 X^3$, and $\sigma^{11(e)} = C^{1111} \epsilon_{11}^{(e)} = k_3 X^3$, while other components are zero. k_1, k_2 and k_3 are some constant parameters.

4.1 Primal formulation

Taking into account the above assumptions, and by employing the identities $d\Gamma = d\Gamma_0 dX^3$ and $d\Omega = d\Omega_0 dX^3$, the LWF (21) associated with an internal node couple I assumes the form

$$\int_{L_s^I} n_\gamma \sigma^{i\gamma} d\Gamma = \int_{-\frac{h}{2} L_{s0}^I}^{\frac{h}{2}} \int n_\gamma C^{i\gamma kl} \frac{1}{2} \left(u_{,X^l}^k + u_{,X^k}^l \right) d\Gamma_0 dX^3 = 0, \quad (27)$$

$$\begin{aligned}
 \int_{L_s^l} X^3 n_\gamma \sigma^{i\gamma} d\Gamma - \int_{\Omega_s^l} \sigma^{i3} d\Omega &= \int_{-\frac{h}{2}}^{\frac{h}{2}} \int_{L_{s0}^l} X^3 n_\gamma C^{i\gamma kl} \frac{1}{2} \left(u_{,X^l}^k + u_{,X^k}^l \right) d\Gamma_0 dX^3 - \\
 &\int_{-\frac{h}{2}}^{\frac{h}{2}} \int_{\Omega_{s0}^l} C^{i3kl} \frac{1}{2} \left(u_{,X^l}^k + u_{,X^k}^l \right) d\Omega_0 dX^3 = 0.
 \end{aligned} \tag{28}$$

In the above relations, Ω_{s0}^l denotes the intersection between Ω_s^l and the X^1, X^2 -plane, while L_{s0}^l is the intersection between $\partial\Omega_s^l$ and the X^1, X^2 -plane, as illustrated in Fig. 3.

By inserting the displacements (11) and by setting $\mathbf{v} = 0$, and after integrating over the thickness, relation (28) may be expanded into the following three relations

$$\begin{aligned}
 \int_{L_{s0}^l} \left[n_1 C^{1111} u_{(1),X^1}^1 + n_2 C^{1212} \left(u_{(1),X^2}^1 + u_{(1),X^1}^2 \right) \right] d\Gamma_0 - \\
 \frac{12}{h^2} \int_{\Omega_{s0}^l} \left[C^{1313} \left(u_{(0),X^1}^3 + u_{(1)}^1 \right) \right] d\Omega_0 = 0,
 \end{aligned} \tag{29}$$

$$\begin{aligned}
 \int_{L_{s0}^l} \left[n_1 C^{1212} \left(u_{(1),X^2}^1 + u_{(1),X^1}^2 \right) + n_2 C^{2222} u_{(1),X^2}^2 \right] d\Gamma_0 - \\
 \frac{12}{h^2} \int_{\Omega_{s0}^l} \left[C^{2323} \left(u_{(0),X^2}^3 + u_{(1)}^2 \right) \right] d\Omega_0 = 0,
 \end{aligned} \tag{30}$$

$$\int_{L_{s0}^l} \left[n_1 C^{3113} \frac{1}{2} u_{(1),X^1}^3 + n_2 C^{3223} \frac{1}{2} u_{(1),X^2}^3 \right] d\Gamma_0 - \frac{12}{h^2} \int_{\Omega_{s0}^l} \left[C^{3333} u_{(1)}^3 \right] d\Omega_0 = 0. \tag{31}$$

Herein, only the terms C^{ijkl} that are different from zero for $\mathbf{v} = 0$ are retained. Note that the first terms in equations (29) and (30) represent the resultant moments over $\partial\Omega_s^l$ with respect to the axes X^1 and X^2 . They are associated with the strains due to bending,

$$\varepsilon_{\alpha\beta}^{(b)} = \frac{1}{2} \left(u_{(1),X^\beta}^\alpha + u_{(1),X^\alpha}^\beta \right). \tag{32}$$

The second integral terms in relations (29)-(31) act as the penalty functions in the thin limit $h \rightarrow 0$. They take into account the actions of the transversal shear strains $\varepsilon_{\alpha 3}$ and the transversal normal strain component ε_{33} .

From equations (29) and (30), it follows that in the thin plate limit the Kirchhoff-Love condition must be satisfied,

$$h \rightarrow 0 \Rightarrow \epsilon_{\alpha 3} = u_{(0),X^\alpha}^3 + u_{(1)}^\alpha \rightarrow 0. \tag{33}$$

This means that $u_{(1)}^\alpha$ should be equal to the negative value of the slope of the deformed elastic plane $u_{(0),X^\alpha}^3$. The penalty term in (31) results in the following condition,

$$h \rightarrow 0 \Rightarrow \epsilon_{33} = u_{(1)}^3 \rightarrow 0, \tag{34}$$

i.e., no stretching in the thickness direction is allowed. Note that the constraints of the strain field (33) and (34) are in complete accordance with the exact analytical solution given by (26).

We assume that all generalized displacement variables are discretized by using the same MLS approximation functions. Although the MLS functions are actually non-polynomial rational functions, if the fourth-order spline-type weighting function is used, they are C^2 continuous everywhere in the domain, and therefore may be approximated in the neighborhood of every point as the polynomial functions of up to the second order. This assumption is further justified by the fact that the MLS function is able to reproduce any polynomial included in the p-basis exactly due to its reproducibility and consistency features, see e.g. [Atluri (2004)].

By neglecting the higher-order terms, the generalized displacement variables $u_{(0)}^3$ and $u_{(1)}^1$ obtained by the first-order p-basis (2) may then be written as

$$u_{(0)}^{3(h)} \approx D_{000}^3 + D_{010}^3 X^1 + D_{001}^3 X^2, \quad u_{(1)}^1 = D_{100}^1 + D_{110}^1 X^1 + D_{101}^1 X^2. \tag{35}$$

By inserting (35) into the Kirchhoff-Love conditions (33), the following constraints are obtained

$$D_{100}^1 + D_{010}^3 \rightarrow 0, \quad D_{110}^1 \rightarrow 0, \quad D_{101}^1 \rightarrow 0. \tag{36}$$

In the thin limit, $D_{110}^1 \rightarrow 0$ is a spurious constraint, because it implies that the rotations described by $u_{(1)}^1$ are constant along the plate instead of being linear as assumed by (35). From (32), it follows that the bending strains $\epsilon_{11}^{(b)} \rightarrow 0$, which means the zero bending moment. Consequently, the solution locks because no bending is predicted.

In the case of the second-order p-basis, the polynomial approximations for $u_{(0)}^3$ and $u_{(1)}^1$ are

$$\begin{aligned} u_{(0)}^{3(h)} &\approx D_{000}^3 + D_{010}^3 X^1 + D_{001}^3 X^2 + D_{020}^3 (X^1)^2 + D_{011}^3 X^1 X^2 + D_{002}^3 (X^2)^2, \\ u_{(1)}^{1(h)} &\approx D_{100}^1 + D_{110}^1 X^1 + D_{101}^1 X^2 + D_{120}^1 (X^1)^2 + D_{111}^1 X^1 X^2 + D_{102}^1 (X^2)^2. \end{aligned} \quad (37)$$

After setting (37) into the Kirchhoff condition (33), it can be easily conducted that one of the constraints on the displacement field is $D_{120}^1 \rightarrow 0$. In a general case, this is a spurious constraint because it leads to the linear distribution of rotations along the plate, instead of the expected quadratic one, and decreases the expected theoretical convergence rates. Nevertheless, for the pure bending of a thin plate the exact solutions can be reproduced accurately, because the rotations are linear and the deflection quadratic according to (26). These findings are confirmed latter in the numerical examples.

It can be concluded that, similarly to FEM, raising the order of the p-basis might alleviate shear locking in the primal approach. However, the sub-optimal convergence rates are to be expected because of the existence of the spurious field constraints in the thin limit. In addition, this technique is computationally inefficient, because of the considerable computational costs needed to calculate the MLS functions of a high order. As explained in [Tiago and Leitão (2007)], using the consistency approach to construct the rotation field shape functions by the direct differentiation of displacements shape functions may result in a rank deficient global system of equations. On the other hand, applying the p-bases of different order to approximate various generalized displacements is also not a suitable approach, because of the prohibitively high computational costs needed for constructing different MLS functions at each integration point. Therefore, it seems that the consistency approach is not appropriate for deriving efficient locking-free primal meshless methods.

It should be stressed that the presented analysis does not lead to quite exact conclusions about the primal meshless formulations because of the non-polynomial character of meshless functions. Further deviations from the theoretical considerations can arise due to the inaccurate numerical integration, which is inherent to all meshless methods based on weak forms.

4.2 Mixed approach

The displacement and strain fields are distributed according to (23), and the assumptions set up for the primal approach are adopted. After integrating over the thickness, the second expression in (21) may be expanded for an internal node cou-

ple in the following form

$$\int_{L'_{s0}} [n_1 C^{1111} (\epsilon_{11(u)} - \epsilon_{11(l)}) + n_2 C^{1212} (\epsilon_{12(u)} - \epsilon_{12(l)})] d\Gamma_0 - \frac{6}{h^2} \int_{\Omega'_{s0}} [C^{1313} (\epsilon_{13(u)} + \epsilon_{13(l)})] d\Omega_0 = 0, \tag{38}$$

$$\int_{L'_{s0}} [n_1 C^{1212} (\epsilon_{12(u)} - \epsilon_{12(l)}) + n_2 C^{2222} (\epsilon_{22(u)} - \epsilon_{22(l)})] d\Gamma_0 - \frac{6}{h^2} \int_{\Omega'_{s0}} [C^{2323} (\epsilon_{23(u)} + \epsilon_{23(l)})] d\Omega_0 = 0, \tag{39}$$

$$\int_{L'_{s0}} [n_1 C^{1313} (\epsilon_{13(u)} - \epsilon_{13(l)}) + n_2 C^{2323} (\epsilon_{23(u)} - \epsilon_{23(l)})] d\Gamma_0 - \frac{6}{h^2} \int_{\Omega'_{s0}} [C^{3333} (\epsilon_{33(u)} + \epsilon_{33(l)})] d\Omega_0 = 0. \tag{40}$$

Like in the primal formulation, the second terms in the above equations act as the penalty functions,

$$\frac{6}{h^2} \int_{\Omega'_{s0}} [C^{i3i3} (\epsilon_{i3(u)} + \epsilon_{i3(l)})] d\Omega_0, \quad i = 1, 2, 3, \text{ no summation over } i. \tag{41}$$

In the thin limit, the following conditions should be fulfilled,

$$h \rightarrow 0 \Rightarrow \int_{\Omega'_{s0}} [C^{i3i3} (\epsilon_{i3(u)} + \epsilon_{i3(l)})] d\Omega_0 \rightarrow 0. \tag{42}$$

According to (4), the strain field is discretized by the MLS functions as

$$\epsilon_{ij(u)}^{(h)}(X^\delta) = \sum_{J=1}^n \phi^J(X^\delta) \hat{\epsilon}_{ij(u)}^J, \quad \epsilon_{ij(l)}^{(h)}(X^\delta) = \sum_{J=1}^n \phi^J(X^\delta) \hat{\epsilon}_{ij(l)}^J, \tag{43}$$

where ϕ^J is the 2-D MLS shape function in the in-plane coordinates X^δ , while $\hat{\epsilon}_{ij(u)}^J$ and $\hat{\epsilon}_{ij(l)}^J$ are the nodal strain values at the upper and lower plate surface,

respectively. By applying (43), the conditions (42) may be transformed to their discretized form as

$$h \rightarrow 0 \Rightarrow \sum_{J=1}^n \left\{ \left[\int_{\Omega'_{s0}} [C^{i3i3} \phi_J(X^\delta)] d\Omega_0 \right] (\hat{\epsilon}_{i3(u)}^J + \hat{\epsilon}_{i3(l)}^J) \right\} \rightarrow 0. \quad (44)$$

By recalling that the MLS functions are able to reproduce the zero strain field, it is clear that the restriction (44) will surely be satisfied exactly if the following conditions are fulfilled at each node couple in the limit,

$$h \rightarrow 0 \Rightarrow \hat{\epsilon}_{13(u)}^J + \hat{\epsilon}_{13(l)}^J \rightarrow 0, \quad \hat{\epsilon}_{23(u)}^J + \hat{\epsilon}_{23(l)}^J \rightarrow 0, \quad \hat{\epsilon}_{33(u)}^J + \hat{\epsilon}_{33(l)}^J \rightarrow 0, \quad (45)$$

for $\forall X_J^\alpha; J = 1, 2, \dots, N$.

For a rectangular plate with $\theta^i = X^i$ and $\mathbf{G}_i = \mathbf{e}_i$, the nodal strains are calculated from the approximated displacements by (12) as

$$\epsilon_{ij} = \frac{1}{2} \left(\frac{\partial u^{i(h)}}{\partial X^j} + \frac{\partial u^{j(h)}}{\partial X^i} \right). \quad (46)$$

Inserting (46) into (45), the approximated displacement field variables must comply with the following constraints

$$h \rightarrow 0 \Rightarrow \begin{cases} u_{(1)}^{1(h)} + u_{(0),X^1}^{3(h)} \rightarrow 0 \\ u_{(1)}^{2(h)} + u_{(0),X^2}^{3(h)} \rightarrow 0, \\ u_{(1)}^{3(h)} \rightarrow 0 \end{cases} \quad \text{for } \forall X_J^\alpha; J = 1, 2, \dots, N. \quad (47)$$

It can be concluded that the penalty functions (41) can be exactly satisfied by fulfilling the conditions (47) only at the node couples, under the condition that the strain field are reproduced accurately. Furthermore, by comparing (47) with (33) and (34), it is obvious that in the mixed strategy the Kirchhoff-Love conditions have to hold only at the node couples, while in the primal approach they have to be satisfied at each sample point of the computational domain. It is also important to note that relations (47) do not produce the spurious constraints for the displacement field, because they only have to be enforced numerically at the certain points, i.e., the nodes. In that case, the system will not lock even if the low-order MLS functions are used. However, certain pathological behavior may manifest due to the non-compatibility of strains and displacements at each point in the global domain, as demonstrated by the numerical examples presented in the following section.

5 Numerical examples

In the following presentation of results, the labels of the types MLSX and IMLSX are used extensively. Thereby, MLS denotes the approximations obtained by using the fourth-order MLS weighting function, while IMLS corresponds to the interpolating MLS functions described in [Sorić and Jarak (2010)]. The label X defines the order of the p-basis.

In all examples, a uniform discretization is used, with the nodal distances in the directions of the parametric coordinate axes θ^α denoted as d_α . The sizes of the parallelepiped Ω_s^I are defined by $d_{T1} = 0,5d_1$ and $d_{T2} = 0,5d_2$, where d_{T1} and d_{T2} denote the half-lengths of the sides of Ω_s^I in the direction of the parametric axes θ^1 and θ^2 , respectively. The support domains of the MLS nodal shape functions are circles in the parametric θ^1, θ^2 – plane. The support domain radii are set to $R_{1r} = 1.3d$, $2.3d$ and $R_{3r} = 3.3d$ for the 1st-, 2nd- and 3rd-order MLS p-basis, respectively, with $d = \max(d_1, d_2)$.

5.1 Cantilever plate

In this study, the bending of a cantilever plate is examined. The length of the plate is fixed at $L = 100$, and the width is $B = 10$. The Young’s modulus of the material is $E = 200000$ and the Poisson’s ratio is $\nu = 0.0$. For discretization purpose, uniform distributions of node couples in the directions of the global axes X^1 and X^2 are used.

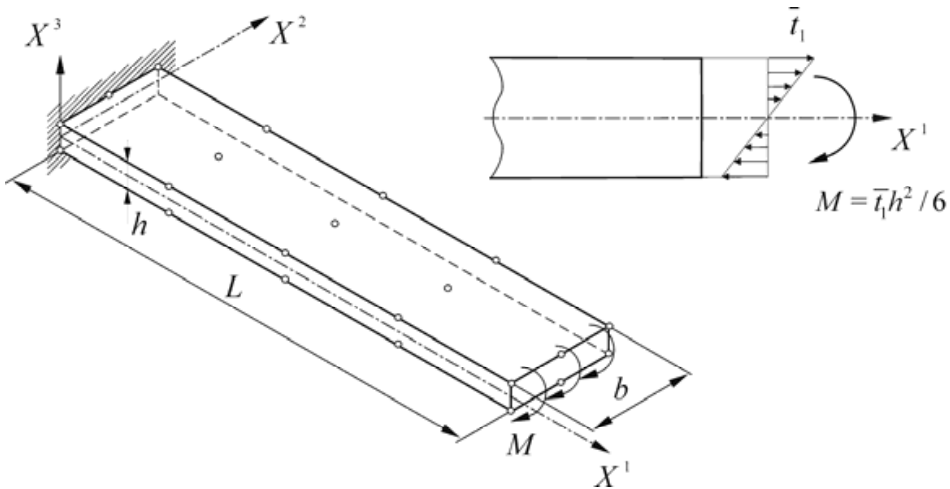


Figure 4: Cantilever plate under pure bending (CP-PB)

5.1.1 Pure bending of thin cantilever plate (CP-PB)

A thin cantilever plate with the thickness $h = 1$, subjected to pure bending is analyzed first. The moment M is obtained by the continuous load $\bar{t}_1 = 10$ at the free end, as shown in Fig. 4, and is equal to $M = \bar{t}_1 h^2 / 6$. According to [Timoshenko and Goodier (1970)], the analytical solution for this problem is

$$u_{(3)a}^0 = w_a = -\frac{MbL}{2EI} (X^1)^2, \quad u_{(1)a}^1 = \varphi_a = \frac{MbL}{EI} X^1, \quad u_{(0)a}^1 = u_{(0)a}^2 = u_{(2)a}^1 = u_{(1)a}^3 = 0. \quad (48)$$

The displacement variables $u_{(3)a}^0$ and $u_{(1)a}^1$ correspond to the classical Euler beam theory for deflection w_a and rotation $\varphi_a = -\partial w_a / \partial X^1$, respectively. I represents the axial moment of inertia of the plate cross section.

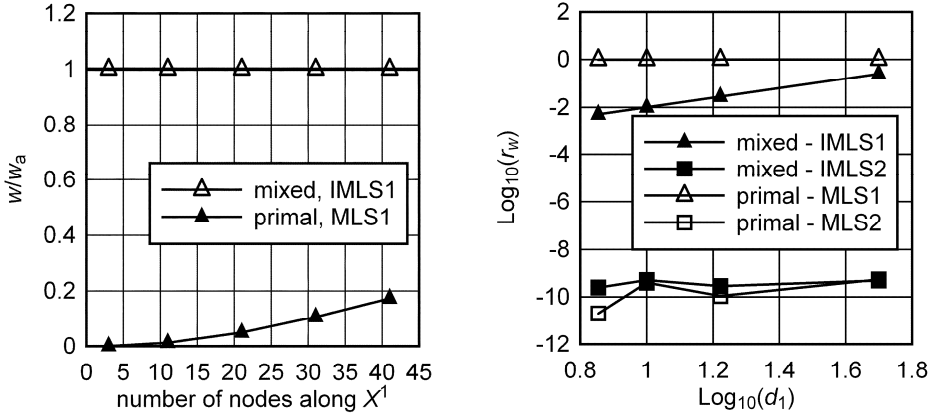


Figure 5: Convergence study for CP-PB: Deflection at the free end of the plate (left), the convergence rate for deflections (right)

The convergence of the deflection at the free end, as well as the convergence rates, is depicted in the Fig. 5. The primal and mixed approaches using the first-order MLS basis are applied. For the convergence rate study, the relative deflection error in L_2 -norms is used, computed by the relation

$$r_w = \frac{\|w_n - w_e\|_{L_2}}{\|w_e\|_{L_2}}. \quad (49)$$

Herein, the L_2 -error is defined as

$$\|w\|_{L_2} = \left(\int_{\Omega} w^2 d\Omega \right)^{1/2} \quad (50)$$

It may be seen that the primal approach produces large errors and converges very slowly to the exact solution, indicating the strong locking behavior. On the other hand, a nearly exact value is obtained by the mixed approach even for few node couples. However, the closer inspection of the error of displacement L_2 -norms reveals that the second-order MLS basis is needed in both the primal and mixed approach to obtain the exact overall solutions, which is consistent with the findings of other researchers, like [Wang and Chen (2004)].

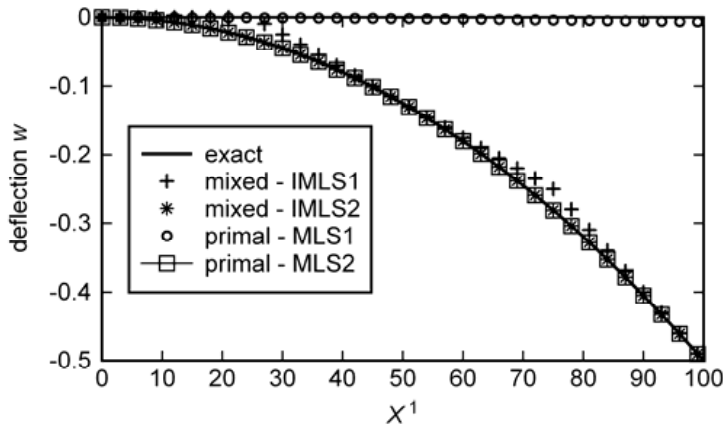


Figure 6: Distribution of deflections w along the plate for CP-PB

The distributions of deflections are given in Fig. 6 for the model with five node couples in the direction of X^1 axis. It is clear that the primal approach yields the excessively rigid response due to locking if the first-order basis is used, while the mixed approach is able to simulate bending relatively accurately. Both formulations achieve very accurate solutions if the second-order p-basis is applied, indicating the complete absence of shear locking.

The convergence rates for the transversal shear force Q^1 and the bending moment M^{11} , defined as

$$Q^1 = \int_{-\frac{h}{2}}^{\frac{h}{2}} \sigma^{13} dX^3, \quad M^{11} = \int_{-\frac{h}{2}}^{\frac{h}{2}} \sigma^{11} X^3 dX^3, \tag{51}$$

are presented in Fig. 7. The results show that the accurate M^{11} and Q^1 are predicted in the mixed approach, while large errors are present in the primal algorithm if the first-order p-basis is employed.

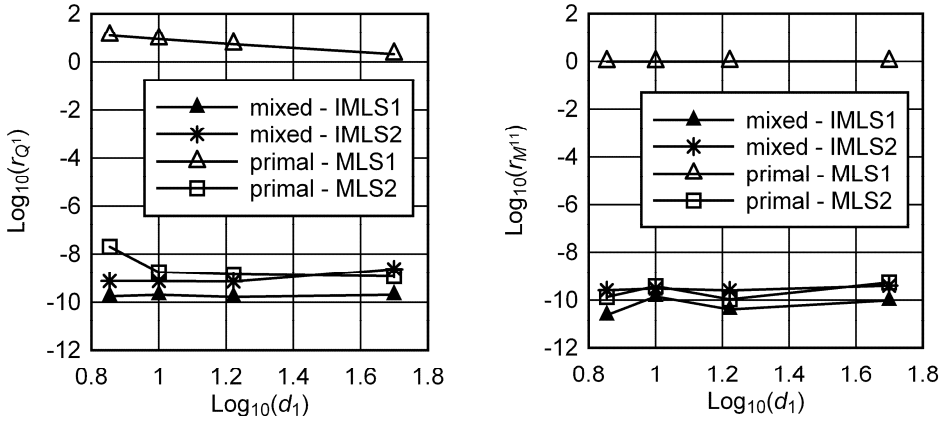


Figure 7: Convergence rates of Q^1 (left), and M^{11} (right) for CP-PB

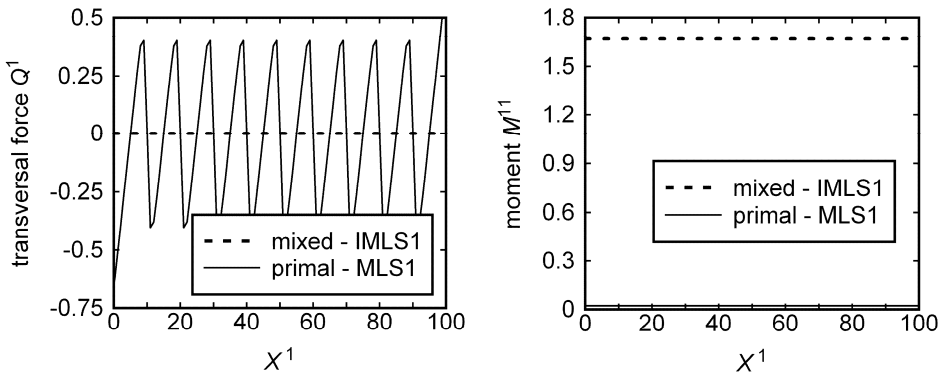


Figure 8: Distribution of Q^1 and M^{11} along the plate for CP-PB - 1st-order MLS basis

Fig. 8 presents the distributions of Q^1 and M^{11} for the first-order p-basis. The model with five node couples in the direction of X^1 axis is used.

In the mixed approach, the zero Q^1 and the constant M^{11} are reproduced exactly. On the other hand, the primal formulation exhibits the significant oscillations of Q^1 . It has been found out by numerical experiments that the amplitude of these oscillations becomes larger when the number of node couples in the X^1 -direction is increased. Furthermore, M^{11} predicted by the primal formulation is close to zero, which confirms the theoretical considerations presented in section 4.1. These findings are analogous to the observations made about comparable FEM formulations,

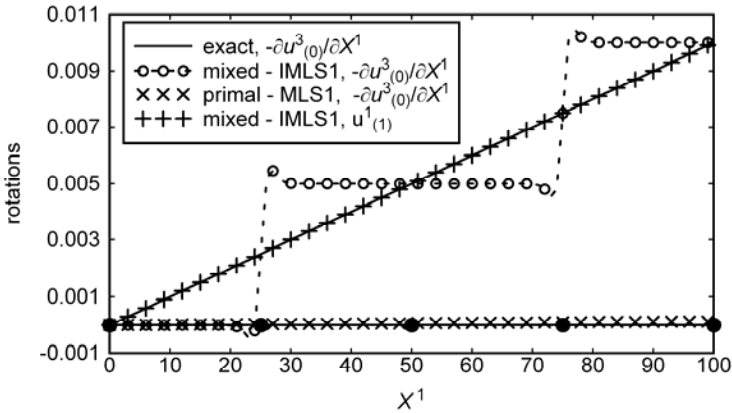


Figure 9: Distribution of rotations along the plate for CB-PB - 1st-order MLS basis

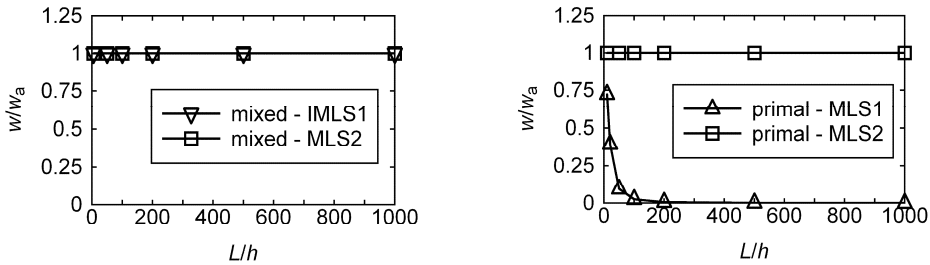


Figure 10: Shear locking test for CP-PB

as noted in [Prathap (1993)].

The distribution of rotations of the deformed elastic plane are plotted in Fig. 9. Only the first-order p-basis is used, and the exact slope of the deformed elastic line, computed as $-\partial u^3_{(0)}/\partial X^1$, is compared to the numerical results, as well as to $u^1_{(1)}$ obtained by the mixed approach. The variable $u^1_{(1)}$ describes the total rotations of the middle surface normal vectors. Again, only five node couples are used in the X^1 -direction. Their position is depicted in the figure by filled circles.

Recall that, according to (48), $u^1_{(1)} = \varphi = -\partial u^3_{(0)}/\partial X^1$. In the primal formulation, $-\partial u^3_{(0)}/\partial X^1$ is close to zero, indicating the pronounced locking effects. The linear distribution of $u^1_{(1)}$ is approximated exactly by the mixed approach, the, i.e. $u^1_{(1)} = \varphi_a$. On the other hand, the slope $\partial u^3_{(0)}/\partial X^1$ is computed accurately only at the node couples, because the zero transversal shear strains ϵ_{13} and the variable $u^1_{(1)}$ may be

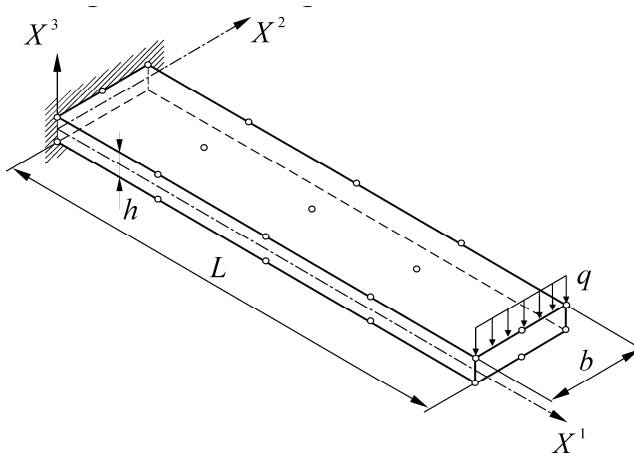


Figure 11: Cantilever plate under a line load at the free end (CP-LL)

predicted correctly by the MLS functions employing the first-order p-basis. Since the compatibility between the approximated strains and displacements is enforced only at the nodes by (25), the Kirchhoff-Love assumptions are satisfied only at these points, according to (47). Nevertheless, as the number of nodes in the model increases, the Kirchhoff-Love conditions are satisfied at more and more points, and the model converges to the exact solutions, as indicated by Fig. 5.

The sensitivity on the shear locking effect has been tested by checking the deflection at the free end of the plate for different length-to-thickness ratios. The results of the test are presented in Fig. 10. As expected, the primal approach employing the first-order p-basis suffers from locking, while no deterioration of accuracy is observed for other settings.

5.1.2 Thin cantilever plate under a transversal line load at the free end (CP-LL)

A thin cantilever plate is subjected to the transversal line load of $q = 0.005$ with the resultant value $P = qb$ at the free end, as shown in Fig. 11. The geometry of the plate is the same as in the previous example.

The analytical solution for $v = 0.0$ may be obtained from [Timoshenko and Goodier (1970)] as

$$\begin{aligned}
 u^1 &= \frac{P(L-X^1)^2 X^3}{2EI} - \frac{P(X^3)^3}{6IG} - \left(\frac{PL^2}{2EI} - \frac{Ph^2}{8IG} \right) X^3, \quad u^2 = 0, \\
 u^3 &= \frac{P(L-X^1)^3}{6EI} - \frac{PL^2(L-X^1)}{2EI} + \frac{PL^3}{3EI}.
 \end{aligned}
 \tag{52}$$

The exact transversal shear forces Q^1 are constant along the plate, while the bending moments M^{11} are distributed in a linear fashion in the X^1 -direction. For $G \rightarrow \infty$ or for $h/L \rightarrow 0$, relations (53) yield the solutions for the classical Euler beam.

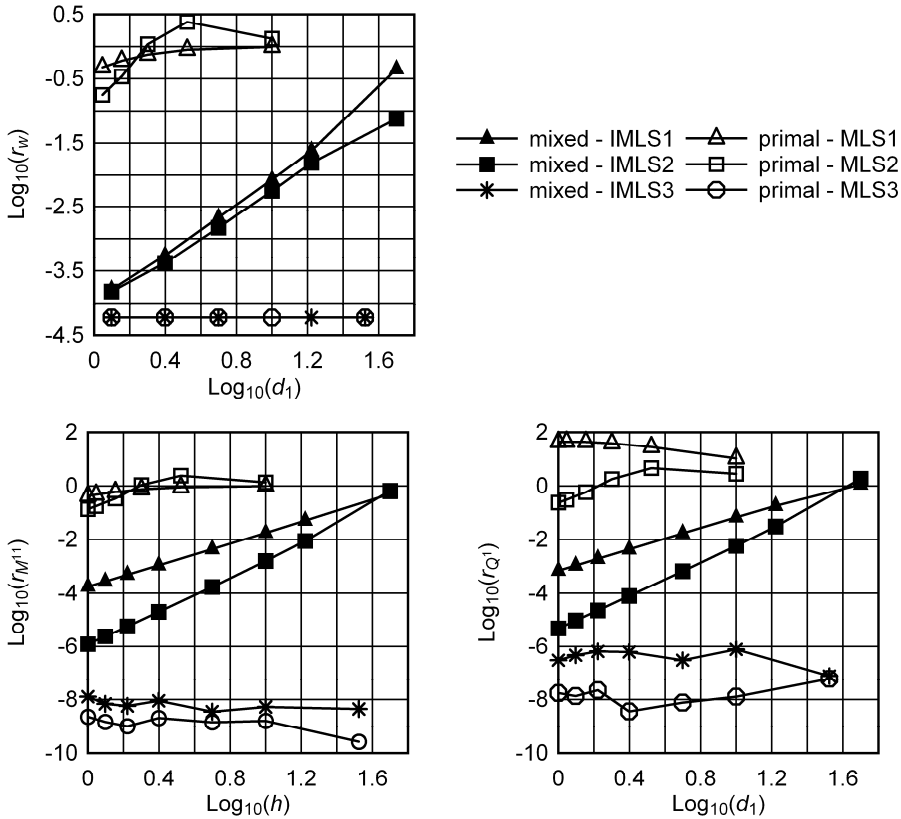


Figure 12: Convergence study for CP-LL

The results of the convergence study are given in Fig. 12. Therein, the relative errors r_w , $r_{M^{11}}$ and r_{Q^1} in L_2 -norms are used for w , M^{11} and Q^1 , respectively, and are defined analogously as in (49) and (50). M^{11} and Q^1 are given by (51), and w is the displacement at the middle surface, $w = u_{(0)}^3$. d_1 is the nodal distance in the X^1 -direction.

The results illustrate that in the primal approach the third-order p-basis is needed to overcome locking, while lower-order p-bases yield large errors and slow convergence rates. It is to note that the second-order p-basis produces better convergence rate and accuracy than the first-order basis only for the larger number of nodes. In

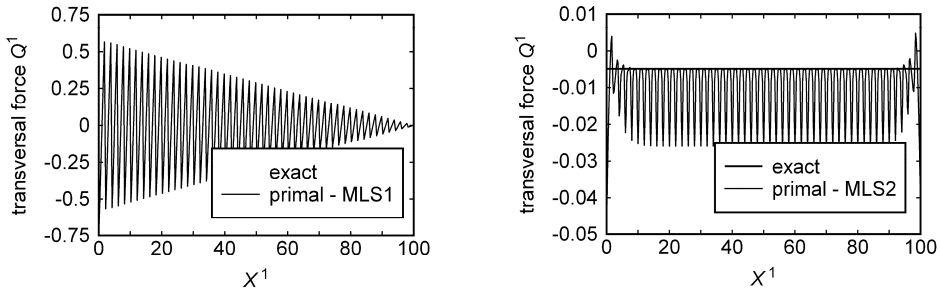


Figure 13: Distribution of Q^1 along CP-LL for the primal approach

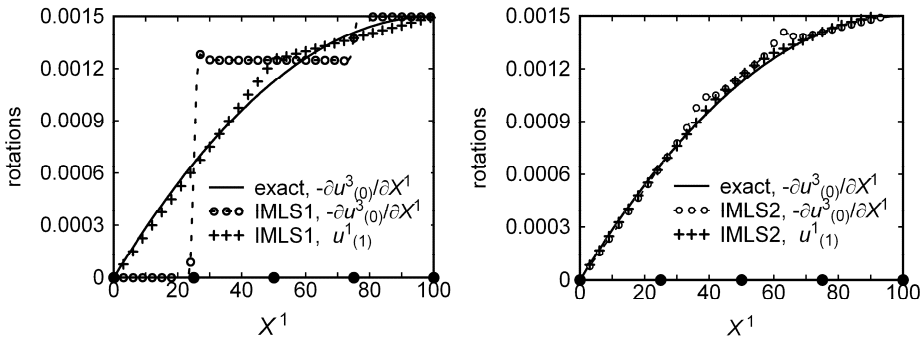


Figure 14: Distribution of rotations along CP-LL for the mixed approach

both cases, Q^1 exhibit wild oscillations, as shown in Fig. 13 for the model employing 51 node couples in the X^1 -direction.

The distribution of rotations for the mixed approach is plotted in Fig. 14. Five nodes are again used along the sides of the model, and their position is indicated in the figure by filled circles. For this problem, $u^1_{(1)}$ is not predicted correctly by the first-order p-basis, because the exact analytical solution for $-\partial u^3_{(0)}/\partial X^1$ is given by a quadratic polynomial in X^1 , according to (52). In the case of the second-order p-basis, the computed slope $-\partial u^3_{(0)}/\partial X^1$ exhibits certain errors due to the lack of global compatibility between the approximated strains and displacements. In general, the rotations will be accurate only at the nodes under the condition that $u^1_{(1)}$ can be computed correctly by the applied approximations.

Fig. 15 presents the distributions of deflections $w = u^3_{(0)}$, bending moments M^{11} and transversal shear forces Q^1 obtained by applying various p-bases in the mixed approach. Again, five equidistant node couples along the plate are used. Their

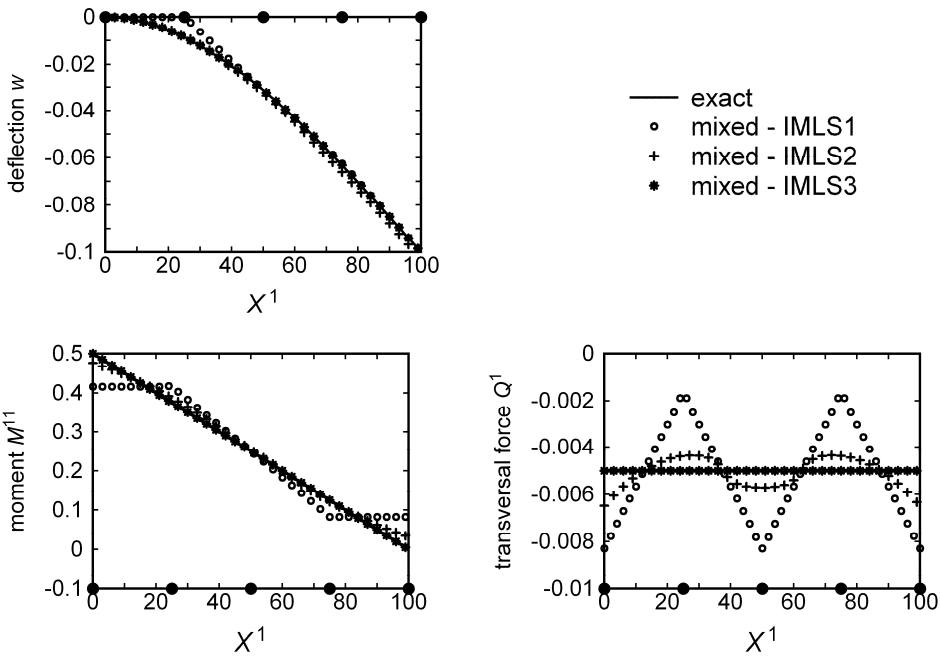


Figure 15: Distribution of w , M^{11} and Q^1 along CP-LL for the mixed approach

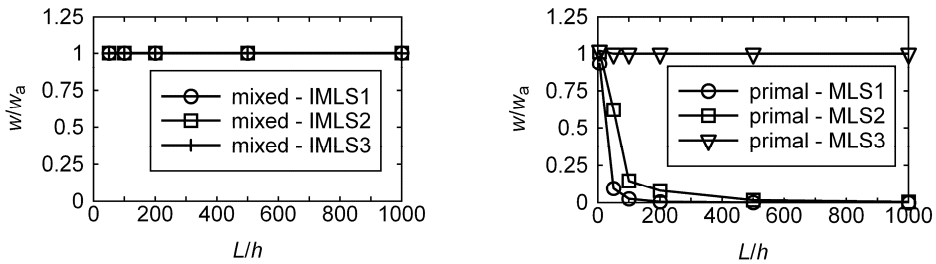


Figure 16: Shear locking test for CP-LL

position is indicated in Fig. 15 by filled circles. Relatively good agreement with the exact analytical solution is obtained for w and M^{11} . As can be seen, Q^1 exhibits oscillations around the exact value for the first- and second-order p-bases. They might arise because the first- and second-order p-bases cannot represent the exact deflection, which is a third-order polynomial along the X^1 -axis according to (52). Numerical experiments have confirmed that these oscillations decrease quickly by increasing the number of node couples along the plate. As expected, the third-order

p-basis yields exact solutions.

The shear locking test is again performed by checking w at the free end for different plate length-to-thickness ratios and the results are presented in Fig. 16. As expected, the primal approach with the first- and second-order p-bases suffers from severe locking, while accurate solutions are obtained in other cases.

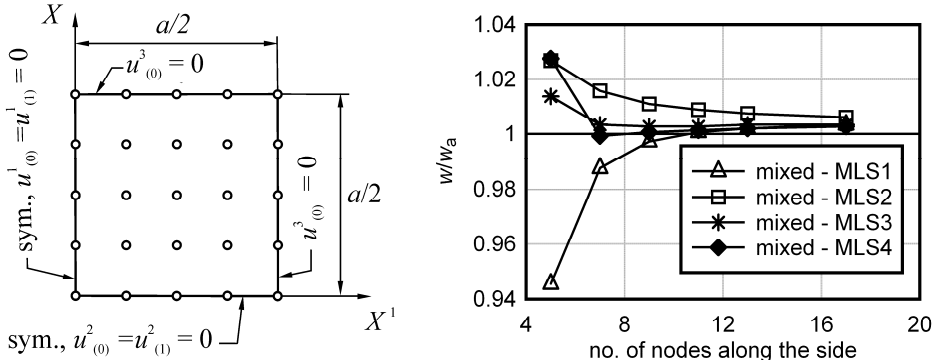


Figure 17: BCs, discretization and convergence of the centre point for SSSP-CL

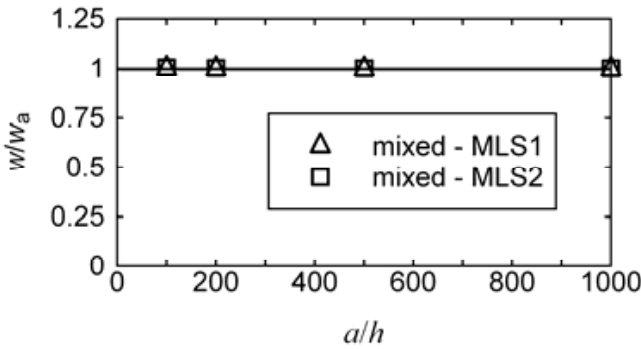


Figure 18: Shear locking test for the SSSP-CL

5.2 Simply supported square plate under centre point load (SSSP-CL)

A thin square plate is supported along all boundary edges and is loaded by the concentrated force $F = 4$ at the center. The side length of the plate is fixed at $a = 100$. The Poisson's ratio is $\nu = 0.3$ and the Young's modulus is $E = 200000$. Due

to symmetry, one quadrant of the plate is discretized by uniform grids, as shown in Fig. 17. The same figure displays the convergence of the central deflection w for the mixed formulation. The thickness locking effect is removed by applying the procedures mentioned in section 3.3. The numerical solutions for w are normalized by the analytical value w_a , obtained from [Timoshenko and Goodier (1970)]. The plate thickness for this test is $h = 1$. As expected, the convergence increases by raising the order of the p-basis, and good accuracy is obtained even for the first-order p-basis. The results of the shear locking test are presented in Fig. 18, and again, shear locking is completely suppressed.

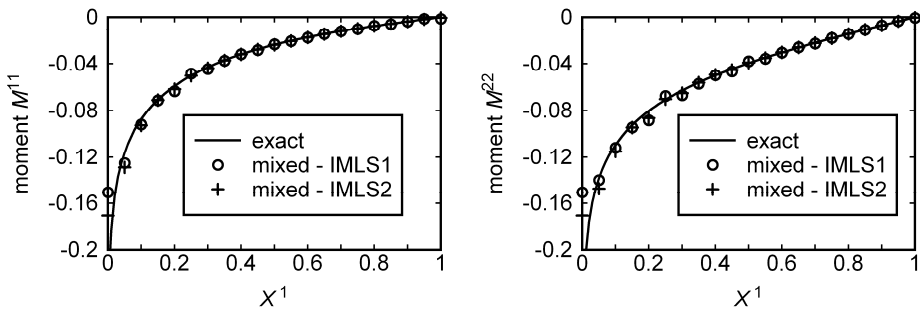


Figure 19: Bending moments along the line $X^2 = 0$ for the SSSP-CL

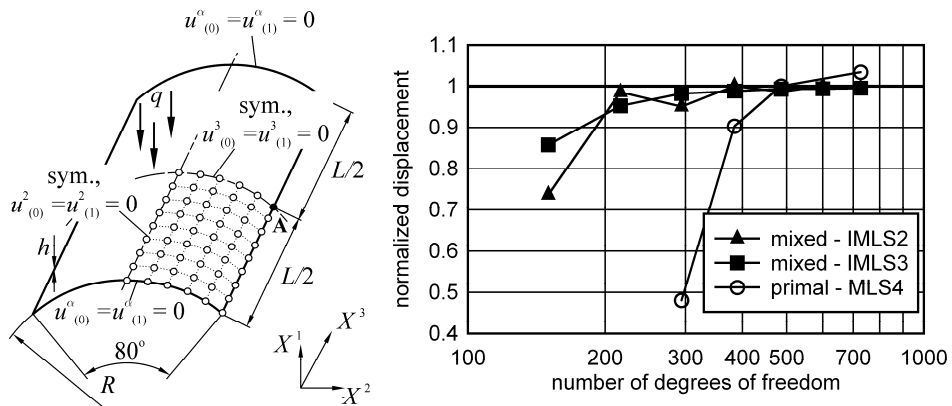


Figure 20: Scordelis-Lo shell roof: Geometry and discretization (left), convergence of vertical displacement at point A (right)

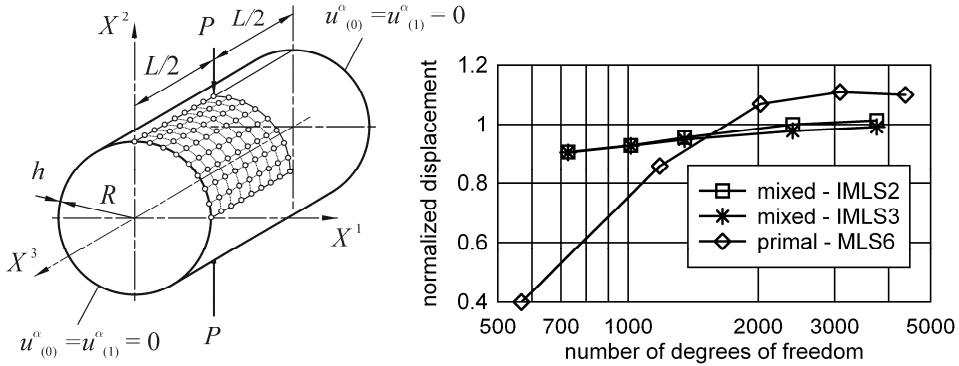


Figure 21: Pinched cylinder: geometry, BCs, and discretization (left), convergence test (right).

The distributions of bending moments along the X^1 coordinate are shown in Figure 19. Along this coordinate the model is discretized by 17 node couples. Very good agreement with the analytical solutions is achieved, but large errors occur in the vicinity of the plate center, where the analytical solution possesses the singularity due to the action of the concentrated load F .

5.3 Scordelis-Lo shell roof

The problem considered in this section is the Scordelis-Lo shell roof, a standard benchmark test in the numerical analysis of shell structures. It is used to test whether shell formulations lock in the thin limit due to the existence of shear or membrane locking. The longitudinal shell edges are free, and the two circular edges are supported by rigid diaphragms, as shown in Fig. 20.

The shell is subjected to the uniform vertical load $q = 4.302 \times 10^{-3}$. The material data are the Young's modulus $E = 2.0684 \times 10^4$ and the Poisson's ratio $\nu = 0.0$. The radius and length of the roof are $R = 7.62$ and $L = 15.24$, respectively, and the radius to thickness ratio is $R/h = 100$. Owing to symmetry, only one quarter of the shell is modeled by applying uniform grids. The right side of Fig. 20 presents the convergence of the normalized vertical displacement at the middle surface point A. The numerical solutions are normalized by the analytical value [MacNeal (1994)]. As expected, the results display the superiority of the mixed formulation over the primal MLPG approach. The mixed algorithm achieves satisfactory convergence even with the second-order p-basis, while the fourth-order basis is necessary to obtain the convergence of the primal formulation.

5.4 Pinched cylinder

The final example analyzed here is a thin cylinder bounded by two rigid diaphragms and pinched by two radial forces $P = 4.482$ in the middle of the structure. In this problem, transversal shear locking is more significant than membrane locking due to the action of the concentrated forces. The geometry, boundary conditions, and the discretization of the shell are presented in Fig. 21.

The Young's modulus is $E = 2.0684 \times 10^5$ and the Poisson's ratio is $\nu = 0.3$. The radius to thickness ratio is $R/h = 100$ with the shell thickness $h = 76.2$. The length of the shell is $L = 15.24$. Due to the symmetry only one octant of the shell is analyzed. The thickness locking effect is eliminated as explained in section 3.3.

The convergence of the vertical displacement under the point load is presented in the diagram in Fig. 21, where the solutions are normalized by using the exact solution from [MacNeal (1994)]. As can be seen, it is sufficient to apply the second-order p-basis to achieve convergence in the mixed approach, while the sixth-order basis is required to obtain a plausible convergence when using the primal algorithm, because of severe shear locking.

6 Conclusion

The solid-shell MLPG approach for the numerical analysis of plates and shells is reviewed, and its behaviour in the structure thin limit is analyzed in detail. According to the solid-shell approach, the couples of nodes positioned on the upper and lower shell surface are used to discretize the shell continuum. The governing equations are derived by defining a local sub-domain around each node couple, and by writing a LWF of the 3-D equilibrium equations over the local sub-domain. The Petrov-Galerkin method is applied, and test and trial functions from different functional spaces are used. The trial functions for unknown field variables are constructed by using the MLS functions in the in-plane directions, while simple polynomials are employed in the thickness direction. In the mixed algorithm, the shear stress components are approximated separately from the displacements. The LWF of the equilibrium equations is written in terms of the approximated strains, and the unknown nodal strains are eliminated from the system of equations by enforcing the 3-D kinematic relations at the nodes.

Special attention has been devoted to the transversal shear locking effect. The theoretical origins of shear locking in the primal approach are revealed by considering the pure bending of rectangular plate in the thin limit, whereby the consistency paradigm is employed. It has been shown that shear locking appears when low-order MLS p-bases are employed. In the case of higher-order p-bases, locking might be alleviated, but in general, sub-optimal convergence rates are to be

expected. The presented numerical experiments clearly demonstrate that such approach is not capable of removing shear locking completely. Moreover, it is numerically inefficient due to the significant costs needed for the evaluation of approximation functions of a high order.

The mechanisms leading to the locking-free behaviour of the mixed MLPG strategy are also explored. Since in this approach the compatibility between the approximated displacements and shear strains is enforced only at the nodes, the Kirchhoff-Love conditions have to be satisfied only at these points to eliminate shear locking completely. In contrast to the primal formulation, this is accomplished without imposing any spurious constraints on the displacement variables that describe the rotation field. The validity of the theoretical predictions is confirmed by the numerical examples. The results indicate that the mixed MLPG approach is superior to the primal MLPG formulations, because the shear locking effects are efficiently suppressed by using the p-bases of a low order. This greatly reduces the computational costs associated with the computation of the MLS approximations. Furthermore, smaller support domains of the shape functions may be used, which results in a narrower bandwidth of the global stiffness matrix, and consequently, enables the faster solution of equations at the global level.

References

- Atluri, S.N.** (2004): *The Meshless Method (MLPG) for Domain & BIE Discretization*, Tech. Science Press.
- Atluri, S.N.; Han, Z.D.; Rajendran, M.J.** (2004). A New Implementation of the Meshless Finite Volume Method, Through the MLPG “Mixed” Approach. *CMES: Computer Modeling in Engineering & Sciences*, vol.6, pp. 491–513.
- Atluri, S. N.; Zhu, T.** (1998): A new meshless local Petrov-Galerkin (MLPG) approach in computational mechanics. *Comput. Mech.*, vol. 22, pp. 117–127.
- Atluri, S.N.; Zhu, T.** (2000): The meshless local Petrov-Galerkin (MLPG) approach for solving problems in elasto-statics. *Comput. Mech.*, vol. 25, pp. 169-179.
- BaniHani, S. M.; De, S.** (2009): On the evaluation of the method of finite spheres for the solution of Reissner-Mindlin plate problems using the numerical inf-sup test. *Int. J. Numer. Meth. Engng.*, vol. 70, pp. 1366-1386.
- Bathe, K.J.** (2001): The inf-sup condition and its evaluation for mixed finite element methods. *Computers and structures*, vol. 79, pp. 243-252.
- Chen, J-S.; Wang, D.** (2006): A constrained reproducing kernel particle formulation for shear deformable shell in Cartesian coordinates. *Int. J. Numer. Meth.*

Engng., vol. 68, pp. 151–172.

Cho J.Y.; Atluri, S.N. (2001): Analysis of shear flexible beams, using the meshless local Petrov-Galerkin method, based on locking-free formulation. *Engineering Computations*, vol.18, pp. 215-240.

De, S.; Bathe, K.J. (2000): The method of finite spheres. *Comput. Mech.*, pp. 329-345.

De, S.; Bathe, K.J. (2001): Displacement/pressure mixed interpolation in the method of finite spheres. *Int. J. Numer. Methods Eng.*, vol. 51, pp. 275-292.

Dolbow, J.; Belytschko, T. (1999): Volumetric locking in the Element Free Galerkin Method. *Int. J. Numer. Meth. Engn.*, vol. 46, pp. 925-942.

Donning, B.M. ; Liu, W.K. (1998): Meshless methods for shear-deformable beams and plates. *Comput. Methods Appl. Mech. Engrg.*, vol. 152, pp. 47-71.

Garcia, O.; Fancello, E.A.; de Barcellos, C.S.; Duarte, C.A. (2000): hp-Clouds in Mindlin's thick plate model. *Int. J. Numer. Meth. Engng.*, vol. 47, pp. 1381-1400.

Han, Z.D.; Rajendran, A.M.; Atluri, S.N. (2005): Meshless Local Petrov-Galerkin (MLPG) Approaches for Solving Nonlinear Problems with Large Deformations and Rotations. *CMES: Computer Modeling in Engineering & Sciences*, vol. 1, pp. 1-12.

Hauptmann, R., Schweizerhof, K. (1998): A systematic development of solid-shell element formulations for linear and non-linear analyses employing only displacement degrees of freedom, *Int. J. Numer. Meth. Engng.*, vol. 42, pp. 49-69.

Hughes, T.J.R. (1987): *The Finite Element Method*. Prentice-Hall, Inc.

Jarak, T.; Sorić, J.; Hoster, J. (2007). Analysis of shell deformation responses by the Meshless Local Petrov-Galerkin (MLPG) approach. *CMES: Computer Modeling in Engineering & Sciences*, vol. 18, pp. 235-246.

Jarak, T.; Sorić, J. (2008). Analysis of rectangular square plates by the mixed Meshless Local Petrov-Galerkin (MLPG) approach. *CMES: Computer Modeling in Engineering & Sciences*, vol. 38, pp. 231-261.

Kanok-Nukulchai, W.; Barry, W.; Saran-Yasoontorn, K.; Bouillard, P. H. (2001): On elimination of shear locking in the element-free Galerkin method. *Int. J. Numer. Meth. Engng.*, vol. 52, pp. 705–725.

Kim, N.H.; Choi, K.K.; Chen, J-S.; Botkin, M.E. (2002): Meshfree analysis and design sensitivity analysis for shell structures. *Int. J. Numer. Meth. Engng.*, vol. 53, pp. 2087–2116.

Kim K.D., Liu, G.Z., Han, S.C. (2005): A resultant 8-node solid-shell element

- for geometrically nonlinear analysis. *Comput. Mech.*, vol. 35, pp. 315-331.
- Klinkel, S.; Grutmann, F.; Wagner, W.** (2006): A robust non-linear solid shell element based on a mixed variational formulation. *Comput. Methods Appl. Mech. Engrg.*, vol. 195, pp. 179-201.
- Krysl, P.; Belytschko, T.** (1996): Analysis of thin shells by the element-free Galerkin method. *International Journal of Solids and Structures*, vol. 33, pp. 3057-3080.
- Lancaster, P.; Salkauskas, K.** (1986): *Curve and surface fitting: an introduction*. Academic Press Ltd.
- Li, S.; Atluri, S.N.** (2008): The Mixed Collocation Method for Material Orientation and Topology Optimization of Anisotropic Solids and Structures. *CMES: Computer Modeling in Engineering & Sciences*, vol. 30, pp. 37-56.
- Li, S.; Hao, W.; Liu, W.K.** (2000): Numerical simulations of large deformation of thin shell structures using meshfree method. *Comput. Mech.*, vol. 25, pp. 102–116.
- Li, Q.; Sorić, J.; Jarak, T.; Atluri, S.N.** (2005): A locking-free meshless local Petrov-Galerkin formulation for thick and thin plates, *Journal of Computational Physics*, vol. 208, pp. 116-133.
- Liu, L.; Chua, L.P.; Ghista, D.N.** (2007): Applications of point interpolation method for spatial general shell structures. *Comput. Methods Appl. Mech. Engrg.*, vol. 196, pp. 1633-1647.
- Liu, L.; Liu, G.R.; Tan, V.B.C.** (2002): Element free method for static and free vibration analysis of spatial thin shell structures. *Comput. Methods Appl. Mech. Engrg.*, vol. 191, pp. 5923–5942.
- MacNeal, R.H.** (1994): *Finite Elements: Their design and performance*. Marcel-Dekker, Inc.
- Most, T.** (2007): A natural neighbour-based moving least-squares approach for the element-free Galerkin approach. *Int. J. Numer. Meth. Engng.*, vol. 71, pp. 224-252.
- Most, T.; Bucher, C.** (2005): A Moving Least Squares weighting function for the Element-free Galerkin Method which almost fulfills essential boundary conditions. *Structural Engineering and Mechanics*, vol. 21, pp. 315-332.
- Moosavi, M.R.; Delfanian, F.; Khelil, A.** (2011): The orthogonal meshless finite volume method for solving Euler-Bernoulli beam and thin plate problems. *Thin-Walled Structures*, vol. 49, pp. 923-932.
- Moosavi, M.R.; Khelill, A.** (2009): Finite volume meshless local Petrov-Galerkin method in elastodynamic problems, *Engineering Analysis with Boundary Elements*, vol. 33, pp. 1016–1021.

- Noguchi, H.; Kawashima, T. ; Miyamura, T.** (2000): Element free analyses of shell and spatial structures, *Int. J. Numer. Meth. Engng.*, vol. 47, pp. 1215-1240.
- Parisch, H.** (1995): A continuum-based shell theory for non-linear applications. *Int. J. Numer. Meth. Engrg.*, vol. 38, pp. 1855-1883.
- Prathap, G.** (1993): *The Finite Element Method in Structural Mechanics: Principles and Practice of Design of Field-Consistent Elements for Structural and Solid Mechanics*. Kluwer Academic Publishers.
- Puso, M.A.; Chen, J.S., Zywicz, E; Elmer, W.** (2007): Meshfree and finite nodal integration methods. *Int. J. Numer. Meth. Engrg.*, vol. 74, pp. 416-446.
- Qian, L.F. ; Batra, R.C.; Chen, L.M.** (2003): Elastostatic Deformations of a Thick Plate by using a Higher-Order Shear and Normal Deformable Plate Theory and two Meshless Local Petrov-Galerkin (MLPG) Methods. *CMES: Computer Modeling in Engineering & Sciences*, vol. 4, pp. 161-175.
- Rabczuk, T.; Areias, P. M. A.; Belytschko, T.** (2007): A meshfree thin shell method for non-linear dynamic fracture, *Int. J. Numer. Meth. Engng.*, vol. 72, pp. 524–548.
- Sladek, J.; Sladek, V., Mang, M.A.** (2002): Meshless formulations for simply supported and clamped plate problems. *Int. J. Numer. Meth. Engng.*, vol. 55, pp. 359–375.
- Sladek, J.; Sladek, V.; Zhang, C.; Krivacek, J.; Wen, P. H.** (2006): Analysis of orthotropic thick plates by meshless local Petrov–Galerkin (MLPG) method. *Int. J. Numer. Meth. Engng.*, vol. 67, pp. 1830-1850.
- Sorić, J.; Jarak, T.** (2010): Mixed Meshless formulation for analysis of shell-like structures. *Comput. Methods Appl. Mech. Engrg.*, vol. 199, pp. 1153-1164.
- Sze, K.Y.** (2002): Three-dimensional continuum finite element models for plate/shell analysis. *Prog. Struct. Engng. Mate.*, vol. 4, pp. 400-407.
- Tan X.G.; Vu-Quoc, L.** (2005): Optimal solid shell element for large deformable composite structures with piezoelectric layers and active vibration control. *Int. J. Numer. Mech. Engng.*, vol. 64, pp. 1981-2013.
- Tiago C.; Leitão, V.** (2007): Eliminating Shear-Locking in Meshless Methods: A Critical Overview and a New Framework for Structural Theories, in *Advances in Meshfree Techniques*, pp. 123-145, Springer, Dordrecht, 2007.
- Timoshenko, S.P., Goodier, J.N.** (1970): *Theory of elasticity, 3rd edition*. McGraw-Hill.
- Wang, D.; Chen, J.-S.** (2004): Locking-free stabilized conforming nodal integration for meshfree Mindlin-Reissner plate formulation. *Comput. Methods. Appl. Mech. Engrg.*, vol. 193, pp. 1065-1083.

Zhu, T.; Atluri, S. N. (1998): A modified collocation method and a penalty formulation for enforcing the essential boundary conditions in the element free Galerkin method. *Comput. Mech.*, vol. 21, pp. 211-222.

Zienkiewicz, O.C.; Taylor, R.L.; Zhu, J.Z. (2005): *The Finite Element Method: Its Basis and Fundamentals, Sixth edition*. Elsevier Butterworth-Heinemann.

